Article

Oxidized Phospholipids Inhibit the Formation of Cholesterol-Dependent Plasma Membrane Nanoplatforms

Mario Brameshuber,[1,*] Eva Sevcsik,[1] Benedikt K. Rossboth,[1] Christina Manner,[1] Hans-Peter Deigner,[2,3] Begüm Peksel,[4] Mária Péter,[4] Zsolt Török,[4] Albin Hermetter,[5] and Gerhard J. Schütz[1,*]

[1]Institute of Applied Physics, TU Wien, Vienna, Austria; [2]Faculty of Medical and Life Sciences, Institute of Precision Medicine, Furtwangen University, Villingen-Schwenningen, Germany; [3]Fraunhofer Institute IZI/EXIM, Furtwangen, Germany; [4]Institute of Biochemistry, Biological Research Centre, Hungarian Academy of Sciences, Szeged, Hungary; and [5]Institute of Biochemistry, Graz University of Technology, Graz, Austria

ABSTRACT We previously developed a single-molecule microscopy method termed TOCCSL (thinning out clusters while conserving stoichiometry of labeling), which allows for direct imaging of stable nanoscopic platforms with raft-like properties diffusing in the plasma membrane. As a consensus raft marker, we chose monomeric GFP linked via a glycosylphosphatidylinositol (GPI) anchor to the cell membrane (mGFP-GPI). With this probe, we previously observed cholesterol-dependent homo-association to nanoplatforms diffusing in the plasma membrane of live CHO cells. Here, we report the release of this homo-association upon addition of 1-palmitoyl-2-(5-oxovaleroyl)-*sn*-glycero-3-phosphocholine (POVPC) or 1-palmitoyl-2-glutaroyl-*sn*-glycero-3-phosphocholine, two oxidized phospholipids (oxPLs) that are typically present in oxidatively modified low-density lipoprotein. We found a dose-response relationship for mGFP-GPI nanoplatform disintegration upon addition of POVPC, correlating with the signal of the apoptosis marker Annexin V-Cy3. Similar concentrations of lysolipid showed no effect, indicating that the observed phenomena were not linked to properties of the lipid bilayer itself. Inhibition of acid sphingomyelinase by NB-19 before addition of POVPC completely abolished nanoplatform disintegration by oxPLs. In conclusion, we were able to determine how oxidized lipid species disrupt mGFP-GPI nanoplatforms in the plasma membrane. Our results favor an indirect mechanism involving acid sphingomyelinase activity rather than a direct interaction of oxPLs with nanoplatform constituents.

INTRODUCTION

Polyunsaturated fatty acids esterified to phospholipids are frequently modified by reactive oxygen species, resulting in biologically active oxidized phospholipids (oxPLs) (1,2). The resulting oxPL stress affects the chemical structures of biomolecules and, as a consequence, signaling cascades triggering pathophysiological effects in the cells of the vascular wall (3). Inflammatory diseases involving oxPLs include neurodegenerative processes, type 2 diabetes, age-related macular degeneration, and cancer (reviewed in Kinnunen et al. (4)). Most importantly, the formation of oxidized low-density lipoprotein (LDL) due to modification of its (phospho)lipid and protein constituents is a hallmark of the development of atherosclerosis (reviewed in Stemmer and Hermetter (2)). Apoptosis of vascular cells is a prominent feature of the late phase of the chronic disease atherosclerosis, which leads to plaque rupture followed by acute vascular events (5,6). We previously showed that both 1-palmitoyl-2-(5-oxovaleroyl)-*sn*-glycero-3-phosphocholine (POVPC), an oxPL carrying an aldehyde group at the truncated chain, and 1-palmitoyl-2-glutaroyl-*sn*-glycero-3-phosphocholine (PGPC), an oxPL carrying a carboxylic group, can induce apoptosis in cultured vascular smooth muscle cells and macrophages (7,8). This phenomenon is causally linked to the fast activation of an acid sphingomyelinase (aSMase), which subsequently generates ceramide, an apoptotic second messenger in these cells (7,8). However, the molecular mechanism of oxPL sensing in the plasma membrane and the consecutive structural changes of the membrane-associated components have remained enigmatic.

We recently found that properties of the plasma membrane of living cells can be altered by incorporating oxPL species containing a carboxy residue at the truncated *sn*-2 chain. PGPC-treated cells showed significantly increased mobility of a tracer lipid, reflecting a PGPC-induced change of the cell membrane viscosity, and dramatic morphological changes within 30 s of treatment (9). Studies on model membranes have shown how oxPLs affect the basic biophysical properties of the host membrane (for a review see Jurkiewicz et al. (10)). The increased lateral diffusion and local mobility of lipids upon addition of various oxPL species could be linked to the orientation of the oxidized lipid chain in the aqueous solution (11). In turn, single-molecule-tracking experiments suggested that diffusion of the fluorescently labeled lipid 1-palmitoyl-2-glutaroyl-*sn*-glycero-3-phospho-N-Alexa647-ethanolamine (PGPE-A647) was twice as high as that of a non-oxPL at

Submitted August 25, 2015, and accepted for publication November 13, 2015.

*Correspondence: brameshuber@iap.tuwien.ac.at or schuetz@iap.tuwien.ac.at

Editor: Joseph Falke.

0006-3495/16/01/0205/9

http://dx.doi.org/10.1016/j.bpj.2015.11.018

37°C in a supported lipid bilayer (12). Interestingly, the difference in mobility was reduced by increasing the cholesterol concentration in the lipid bilayer. Based on molecular-dynamics (MD) simulations, investigators ascribed this effect to an increased interaction of oxPLs with the lipid matrix at high cholesterol levels, thereby pulling the oxPL headgroup closer to the bilayer interface. In addition, recent MD simulation and dynamic light-scattering experiments showed colocalization of cholesterol and oxPL in lipid bilayers (13). Also, Stefl and co-workers (14) found cholesterol rearrangement and preferred interactions with carbonyls of PGPC chains in oxidized model membranes. Micrometer-sized sphingomyelin/cholesterol domains were found to be stabilized in monolayers of ternary lipid mixtures by oxPLs containing an aldehyde or a carboxylic group at the truncated chain (15). It should be noted that the aldehyde derivative was more efficient at stabilizing phase separation, possibly due to the different orientation of the oxidatively truncated acyl chains (16) and therefore an enhanced interaction of the aldehyde derivative with sphingomyelin (15). Additionally, oxPLs with an aldehyde group at the *sn*-2 position proved to be more cytotoxic than those with the carboxylic group (17), probably because of the ability of the aldehyde group to covalently interact with primary amino groups of proteins and amino phospholipids via the formation of Schiff bases (3).

In this work, we aimed to understand the effects of oxPL treatment on the live-cell plasma membrane of Chinese hamster ovary (CHO) cells on the nanoscopic level. Recent advances in imaging techniques have allowed the detection of signaling platforms in the membrane based on their ability to accommodate glycosylphosphatidylinositol (GPI)-anchored proteins (18–22). These nanoplatforms seem to influence signal transduction (23–27), and their disruption can cause signal abrogation or initiation (28,29). At this time, however, it is unclear to what extent the different protein and lipid domains identified in the plasma membrane relate to the concept of a lipid-driven phase separation mediating the formation of more or less stable protein associates, which was the basis for the lipid raft hypothesis (30) (for a discussion, see Klotzsch and Schütz (31)). In fact, a recent study from our lab challenged the view that ordered-phase formation drives the association of GPI-anchored proteins (32).

Using single-molecule microscopy, we previously detected the presence of stable but mobile homo-associates of a model GPI-anchored protein and of another putative raft marker (Bodipy-GM1) diffusing in the plasma membrane of different cell lines (20). In line with other studies (33–36), we chose a minimal GPI-anchored protein, monomeric GFP anchored via GPI to the plasma membrane (mGFP-GPI), which was shown to probe basic membrane properties similar to those probed by its counterparts containing a fully functional extracellular domain (33,34,37). In our previous study (20), we found that ~20–50% of the mGFP-GPIs examined were present as homodimers, which is in line with other fluorescence microscopy approaches that showed a nonhomogeneous plasma membrane distribution of mGFP-GPI on the nanoscale (19,22,33–35,37). Interestingly, cholesterol depletion resulted in a complete disintegration of the observed homo-dimers, indicating that the local lipid environment is a crucial factor for the cohesion of mGFP-GPI assemblies. We termed these cholesterol-dependent mGFP-GPIs homodimer nanoplatforms. Thus, it appeared attractive to hypothesize that molecular interactions between cholesterol and oxPL could also occur in the native plasma membrane and account (at least partly) for oxPL's modes of action.

In this work, we studied the effect of oxPLs on plasma membrane nanoplatforms using single-molecule microscopy. We observed the disintegration of mGFP-GPI nanoplatforms upon addition of PGPC or POVPC. Interestingly, treatment with lysolipids had no effect, ruling out a general alteration of lipid bilayer properties due to the addition of inverted-cone-shaped lipids. The loss of mGFP-GPI homo-association upon POVPC addition correlated with apoptosis signals observed by detecting the amount of phosphatidylserine (PS) in the outer leaflet of the plasma membrane.

MATERIALS AND METHODS

Fusion constructs and cell culture

An mGFP-GPI plasmid carrying the GPI signal sequence of the human folate receptor was constructed as described previously (20). Briefly, the GFP in the GPI-GFP pJB20 plasmid (a kind gift from Jennifer Lippincott-Schwartz) was mutated at amino acid position 206 from alanine to lysine to obtain a monomeric GFP (mGFP) variant (38). CHO cells (ATTC CCL-61) stably transfected with mGFP-GPI were grown in DMEM/HAM's F-12 medium (BE12-719F; Lonza, Switzerland) supplemented with 10% fetal calf serum (F7524; Sigma-Aldrich, St. Louis, MO), 400 μg/mL G418 (P11-012; PAA, Linz Austria), and 100 U/mL penicillin/streptomycin (17-602E; Lonza). Cells were cultured in a humidified atmosphere at 37°C and 5% CO_2 on 10 cm tissue culture plates (64 160; Greiner Bio-One, Kremsmünster, Austria).

Sample preparation

Coverglass slides (#1.5, BB024060SC; Menzel, Braunschweig, Germany) were glued to eight-well Lab-Tek chambers (155411, Nunc; Thermo Fisher Scientific, Waltham, MA) with the use of two-component dental glue (13001001; Picodent, Germany) and washed with 70% isopropanol and sterile water. Confluent CHO cells were harvested using Accutase (00-4555-6; eBioscience, San Diego, CA) and seeded into Lab-Tek chambers at least 24 h before experiments were conducted. Before treatments, cells were washed twice in a 37°C Hanks' buffered salt solution (HBSS) containing calcium and magnesium (BE10-527F; Lonza). A stock solution of 5 mg/mL POVPC (870606P; Avanti Polar Lipids, Alabaster, AL) or 5 mg/mL PGPC (870602P; Avanti Polar Lipids) was prepared in ethanol and injected into a defined volume of HBSS to reach the desired oxPL concentrations. Seeded and treated cells were incubated for 20 min at 37°C before microscopy or lipid extraction experiments were conducted. For aSMase-inhibition experiments, the inhibitor NB-19 (9-(3-{4-[2-(4-methoxy-phenyl)-ethyl]-3,5-dimethyl-piperazine-1-yl}-propyl)-9H-carbazol) was dissolved in ethanol at a concentration of 5 mM. Cells were incubated with 10 μM of NB-19 diluted in HBSS for 30 min at 37°C, washed twice in

HBSS, and incubated with oxPL as described above. For all experiments, the final ethanol concentration did not exceed 1% (v/v) of total incubation volume. This low amount of ethanol had no membrane-perturbing effects. The presence of 0.2% v/v ethanol (NB-19) or 0.44% v/v ethanol (NB-19 + POVPC) did not lead to a detectable change of the dimer fraction compared with nontreated cells (see Fig. 5 *A*). 1-Palmitoyl-2-hydroxy-*sn*-glycero-3-phosphocholine (16:0 Lyso-PC, 855675; Avanti Polar Lipids) was dissolved in ethanol at a final concentration of 10 mM and injected into HBSS to reach the desired incubation concentrations.

For cholesterol-depletion experiments, cells were incubated with 2 U/mL cholesterol oxidase (COase, C8649; Sigma-Aldrich) at 37°C for 20 min. The COase was not removed during the experiments. For aSMase-inhibition experiments, cells were preincubated with 5 μM of NB-19 for 30 min at 37°C and washed twice in HBSS.

Apoptosis assay

Cells were seeded into 96-well tissue culture plates (655 160; Greiner Bio-One) 24 h before experiments. The cells were washed twice with 37°C HBSS and then treated with NB-19 and oxPL as described above. Apoptosis was detected 30 or 90 min after oxPL incubation using the Annexin V-Cy3 kit (APOAC; Sigma-Aldrich). The kit was applied as described in the manufacturer's manual. Readout was performed using a plate reader (Synergy H1; BioTek, Winooski, VT) with the appropriate excitation/emission settings. For every condition, at least four wells were used and the mean fluorescence was calculated.

Microscopy

Single-molecule experiments were performed as described by Brameshuber et al. (20). Briefly, a Zeiss Axiovert 200 microscope equipped with a 100× NA=1.46 Plan-Apochromat (Zeiss, Oberkochen, Germany) was used to excite cells in objective-based total internal reflection fluorescence (TIRF) configuration via the epiport using 488 nm light from an optically pumped semiconductor laser (Sapphire; Coherent, Santa Clara, CA). The power was adjusted to 2–10 kW/cm^2 on the sample. A slit aperture (Thorlabs, Newton, NJ) with a width of ~7 μm in the object plane was used as the field stop. For exact timings, an acousto-optic modulator (Isomet, Springfield, VA) was used. Timing protocols were generated and controlled by an in-house-written program package implemented in LABVIEW (National Instruments, Austin, TX). After the appropriate filtering (dichroic mirror: ZT488/640rpc 2 mm, Chroma, Bellows Falls, VT; emission filter: FF01-538/685-25, Semrock, Rochester, NY), fluorescence images were recorded using a back-illuminated, nitrogen-cooled CCD camera (Roper Scientific Micro Max 1300-PB; PI Acton, Trenton, NJ). The temperature during experiments was maintained at 37°C by means of an in-house-built incubator box equipped with a heating unit and an objective heater (PeCon, Erbach, Germany).

TOCCSL (thinning out clusters while conserving stoichiometry of labeling) (39) experiments were performed as described elsewhere (20). Briefly, after recording a prebleach image with a power density of ~2 kW/cm^2 and an illumination time of $t_{ill} = 2$ ms (Fig. 1, *A* and *D*, pulse *a*), the sample was bleached for $t_{bleach} = 400$ ms with a 5-fold higher power density. After an adjustable recovery time, $t_{recover} = 0.5$–3 s, up to 20 images with a typical delay of 20 ms were recorded with same settings as used for the prebleach image. To confirm that bleaching was complete, an optional experiment was carried out with a recovery time of $t_{recover} = 1$ ms (Fig. 1, *B* and *D*, pulse *b*). Then the recovery time was increased to allow for the reentry of unbleached mGFP-GPI molecules from the shielded region. The first recorded image after the adjustable recovery time, $t_{recover}$ (Fig. 1, *C* and *D*, pulse *c*), was used for brightness analysis (TOCCSL image), and the last image was used to determine the single-molecule brightness of mGFP (Fig. 1 *D*, pulse *d*). Due to the low bleach stability of GFP, the probability of observing more than one active mGFP-GPI per diffraction-limited spot in the last image is negligible (20). The sample sizes for all of the TOCCSL experiments are

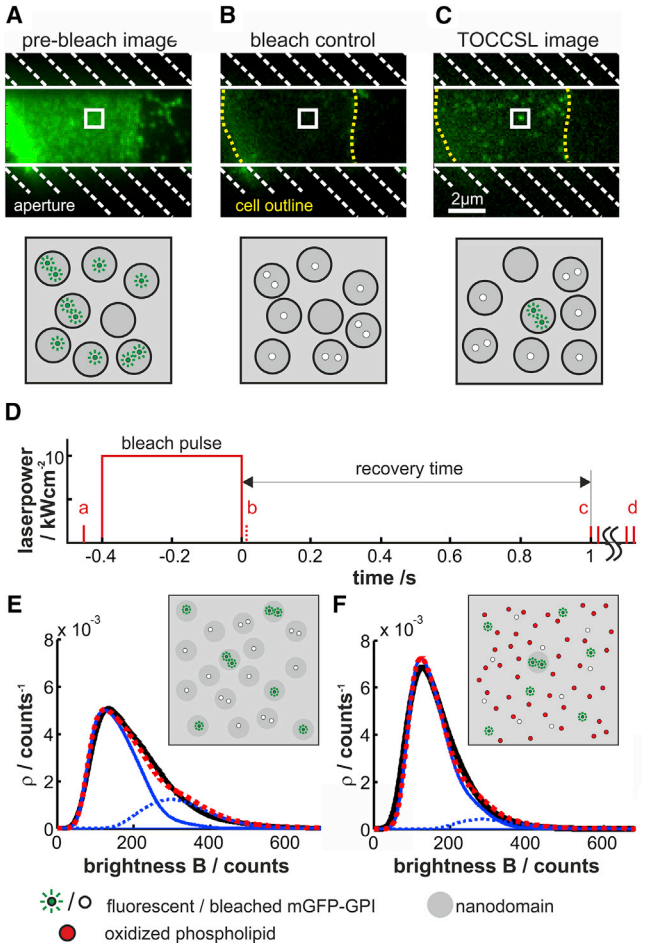

FIGURE 1 Experimental design for detecting nanoplatforms. (*A–C*) The principle of the TOCCSL technique. (*A*) A living CHO cell stably expressing the probe mGFP-GPI. An excitation field stop is used to illuminate only a part of the bottom cell membrane in TIR mode (*dashed area*). The overall density of mGFP-GPI is too high to resolve individual mGFP-GPI nanoplatforms. The sketch displays a high density of nanoplatforms (*black circles*) confining the marker mGFP-GPI. After an ~400-ms-long laser pulse, all mGFP molecules within the observed area become irreversibly photobleached. (*B*) The efficiency of photobleaching was controlled by recording an image 1 ms after the bleach pulse. (*C*) After a recovery time of 1 s, the first fluorescent spots entering the field of view can be observed as diffraction-limited signals. For display, the contrast in (*B*) and (*C*) was increased by a factor of 5 compared with (*A*). The sketch shows an individual recovered nanoplatform, which is now easily resolvable in the presence of bleached mGFP-GPI. (*D*) The corresponding laser-intensity protocol. The letters *a–c* indicate the laser pulses used to record the corresponding images in (*A*)–(*C*), and *d* indicates the laser pulse used to record the image for determining the brightness distribution of individual GFPs, ρ_1 (monomer distribution). (*E* and *F*) The brightness distributions, ρ_N, of single mGFP-GPI spots before (*E*) and after (*F*) addition of 10 μM POVPC are plotted as probability density functions. Data (*black line*) were fitted by Eq. 1 (*red line*). Monomer (*solid*) and dimer (*dashed*) contributions are shown as blue lines. The dimer fraction α_2 was reduced from 30.8% ± 2.5% ($n = 6$ cells) to 8.3% ± 3.3% ($n = 6$ cells) after addition of POVPC. Insets show the putative effect of oxPLs on mGFP-GPI nanoplatforms. All experiments were performed at 37°C. Scale bar: 2 μm.

provided in Table S1 in the Supporting Material. A TOCCSL experiment on one cell could be repeated 20–60 times because for every TOCCSL run, only a small part of the bottom cell membrane was bleached. TOCCSL runs were separated by a delay of 10 s. To control for photophysical effects on membrane constituents due to the high power of the photobleaching pulse, we compared the results of multiple sequential TOCCSL runs on identical cells. We found no change in the mGFP-GPI dimer fraction (Fig. S1). Thus, our data rule out the formation of photo-induced oxPL species during the experiment, which would have led to a decreased dimer fraction (compare with Figs. 2 and 4). In addition, in our previous study (20), we performed control experiments to rule out potential photo-induced cross-linking of mGFP-GPI in the same cell line, and discussed the results in an extensive supplement.

Data analysis

Analysis of TOCCSL recordings was performed as described previously (20). Briefly, algorithms written in-house in MATLAB (The MathWorks, Natick, MA) were used to detect and quantify individual diffraction-limited signals. A maximum-likelihood estimator was used to determine the position, integrated brightness B, full width at half-maximum, and local background of recovered mGFP-GPI signals. Brightness analysis was performed as described previously (39,40). The brightness values of single mGFP-GPI molecules pooled from all cells for one experimental condition were used to calculate the probability density function $\rho_1(B)$ of monomers. Due to the stochastic emission process of photons, the corresponding probability density functions of N colocalized emitters can be calculated by a series of convolution integrals, $\rho_N(B) = \int \rho_1(B')\rho_{N-1}(B - B')dB'$. A linear combination of the resulting brightness distributions was used to calculate a mixed population of monomers and higher-order multimers:

$$\rho(B) = \sum_{N=1}^{N_{max}} \alpha_N \rho_N(B). \quad (1)$$

A minimum of 250–500 brightness values (41) from TOCCSL images of one experimental condition were used to calculate $\rho(B)$. A least-squares fit with Eq. 1 was used to determine the weights of the individual distributions, α_N, with $\sum_{N=1}^{N_{max}} \alpha_N = 1$. For all experiments, no higher contributions than dimers (α_2) were observed. For error-bar estimation, a random 50% subsample of brightness values was drawn from all brightness values from the TOCCSL images and used to calculate α_2. This sampling was repeated 100 times, and the mean and standard deviation (SD) of α_2 were calculated and displayed as error bars. The source code for the MATLAB programs used in this work can be found in the Supporting Material.

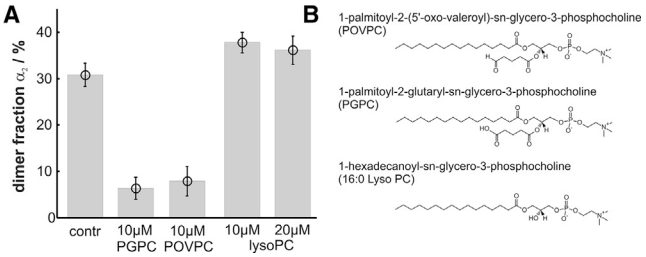

FIGURE 2 Effect of oxPLs on mGFP-GPI nanoplatform integrity. (*A*) CHO cells stably expressing mGFP-GPI were preincubated with the indicated lipids for 20 min. TOCCSL experiments were carried out in the presence of these lipids on a minimum of six cells for each condition. The dimer fraction α_2 decreased substantially upon exposure to the oxPLs PGPC and POVPC. Mock treatment (contr) or incubation with lysolipid had no effect on the integrity of mGFP-GPI nanoplatforms. (*B*) Structure of the lipids used. All experiments were carried out at 37°C.

Lipid extraction and mass spectrometry analysis

A total of 700,000 cells were seeded 24 h before experiments began. After treatment with 10 μM PGPC, 10 μM POVPC, or 10 μM Lyso-PC (as described above), supernatants and cells were collected for subsequent lipid extraction. Trypsinized cells were washed twice with HBSS and the supernatant was completely removed after centrifugation at 4000 rpm for 10 min. Lipids from both the cells and supernatants were extracted in the presence of PC(40:0) as the extraction standard and quantitated by shotgun lipidomic analysis on an LTQ-Orbitrap Elite instrument (Thermo Fisher Scientific, Bremen, Germany) as described in Antal et al. (42).

RESULTS

oxPL species cause disintegration of mGFP-GPI nanoplatforms

We used TOCCSL, a variant of single-molecule microscopy (20,39,41), to detect mGFP-GPI homo-association in the live-cell plasma membrane. The principle of this approach and its putative effect on membrane nanoplatforms are outlined in Fig. 1, *A–C*. CHO cells stably expressing mGFP-GPI were imaged at 37°C with an epifluorescence microscope in TIR mode. The high mGFP-GPI surface density of up to 1000 copies/μm^2 does not allow for the direct detection of mGFP-GPI nanoplatforms, as it results in a rather homogeneous fluorescence distribution on the plasma membrane caused by nanoplatforms spaced closer than the resolution of optical microscopy (Fig. 1 *A*). By applying a high-power laser pulse, we were able to completely photobleach a spatially bounded area of the plasma membrane (Fig. 1 *B*). After a recovery time of 800–2500 ms, we observed a few diffraction-limited signals in the TOCCSL image that had entered the field of view from unbleached parts of the cell by Brownian motion (Fig. 1 *C*). The broad distribution of the brightness values of signals detected in the TOCCSL image is plotted as a probability density function, $\rho(B)$, in Fig. 1 *E*. We quantified the amount of mGFP-GPI molecules per signal by comparison with the brightness of a single mGFP molecule, which we determined in the same experiment upon prolonged photobleaching. For quantification, we fitted $\rho(B)$ with a linear combination of n-mer brightness distributions, $\rho_n(B)$ (Eq. 1), derived from the distribution of single mGFP molecules $(\rho_1(B))$. The weights of the fit (α_n) correspond to the fraction of n-mers (see "Data analysis" section in Materials and Methods). Consistent with our previous study, we found a dimer fraction of $\alpha_2 = 31\% \pm 3\%$, representing two mGFP-GPI molecules stably associated to nanoplatforms (20).

To test the influence of oxPL on nanoplatforms, we incubated mGFP-GPI expressing CHO cells with 10 μM POVPC (for the structure, see Fig. 2 *B*) 20 min before the TOCCSL experiment. A pronounced shift of the brightness distribution, $\rho(B)$, toward the distribution of single mGFP-GPI signals was visible (Fig. 1 *F*). Quantification revealed a reduction of the mGFP-GPI dimer fraction to $8\% \pm 3\%$, i.e., more than 73% of all observed nanoplatforms had

disintegrated (Fig. 2 *A*). The overall surface density of mGFP-GPI was not significantly affected by the presence of oxPL in the plasma membrane (nontreated cells: 389 ± 83 molecules/μm^2, POVPC-treated cells: 337 ± 61 molecules/μm^2).

To further study whether the observed disintegration of mGFP-GPI nanoplatforms is a general effect of oxPLs, we tested PGPC, a different oxPL that carries a carboxylic acid instead of the aldehyde group at the *sn*-2 position (for the structure, see Fig. 2 *B*). mGFP-GPI-expressing cells were incubated with 10 μM PGPC 20 min before the TOCCSL experiment and brightness analysis was performed as described above. We found that the mGFP-GPI nanoplatform fraction was reduced to 6% ± 2%, which is comparable to the decrease observed for POVPC (Fig. 2 *A*). Mock treatment of cells showed no effect.

There are two structural features of oxPL that could be responsible for nanoplatform disintegration: 1) the oxidized fatty acid at the *sn*-2 position, which carries either an aldehyde (POVPC) or a carboxyl (PGPC) group, or 2) the remaining saturated fatty acid at the *sn*-1 position, which bestows an inverse-cone shape to the lipid (9) in contrast to the non-oxPL. To test whether the observed effects were a direct consequence of this geometrical feature of the lipids (e.g., mediated by a change in the pressure profile of the membrane upon integration of noncylindrical lipids), we repeated the experiments using Lyso-PC, a similarly inverted cone-shaped lipid. Lipid mass spectrometry (MS) revealed even higher membrane insertion of Lyso-PC compared with the oxPL probes (Fig. 3). Brightness analysis, however, yielded an unchanged mGFP-GPI dimer fraction of 38% ± 2% (10 μM Lyso-PC) and 36% ± 3% (20 μM Lyso-PC) (Fig. 2 *A*). Apparently, the shape of the added lipids is not responsible for nanoplatform disintegration, so we shifted our focus to a potential functional role of the oxidized *sn*-2 acyl residue in disintegration of mGFP-GPI nanoplatforms.

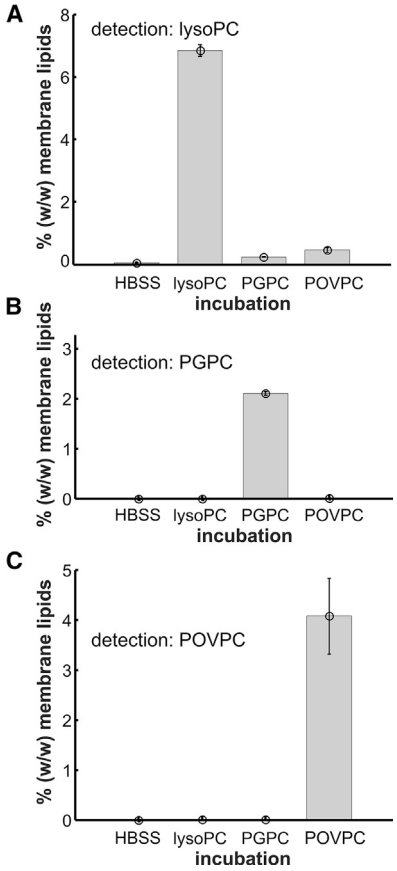

FIGURE 3 Membrane insertion of oxPL and Lyso-PC. CHO cells stably expressing mGFP-GPI were mock treated (HBSS) or incubated with 10 μM Lyso-PC, 10 μM PGPC, or 10 μM POVPC for 20 min at 37°C. After lipid extraction, the lipids were quantitated by MS analysis. (*A–C*) MS quantitation of Lyso-PC (*A*), PGPC (*B*), and POVPC (*C*). Data are presented as means ± SD for three independent measurements.

POVPC-induced mGFP-GPI nanoplatform disintegration correlates with apoptosis

We next examined the dimer fraction with respect to the applied POVPC concentration. For each individual POVPC concentration, we performed a TOCCSL experiment on mGFP-GPI-expressing cells, and the dimer fraction was determined via brightness analysis as described above. We observed the strongest change for POVPC concentrations between 0 and 10 μM (Fig. 4 *A*). For higher concentrations, the dimer fraction did not decrease further; however, morphological changes of the cells were more pronounced and experiments were limited to a duration of 1 h for each data point.

One characteristic function of oxPLs is their ability to trigger apoptosis (8). One can measure apoptosis signals by determining the amount of PS, a negatively charged lipid that is transferred to the outer leaflet of the plasma membrane during apoptosis in a variety of cell types (43). mGFP-GPI-expressing CHO cells were grown in 96-well microtiter plates and incubated with the same concentrations of POVPC as were used for the TOCCSL experiments. We used an Annexin V-Cy3 staining kit to detect negatively charged PS in the plasma membrane 30 min after oxPL incubation. The apoptosis signal increased with increasing oxPL concentrations (Fig. 4 *B*), with the strongest change in the Annexin V-Cy3 signal occurring for POVPC concentrations between 0 and 10 μM, and it correlated with nanoplatform disintegration (Fig. 4 *C*). Measurements obtained 90 min after POVPC incubation yielded similar results, with a slightly increased Annexin V-Cy3 signal at the membrane (data not shown).

Mechanisms of POVPC-induced mGFP-GPI nanoplatform disintegration

There are two possible scenarios for mGFP-GPI nanoplatform disintegration upon incubation with oxPL: 1) a direct

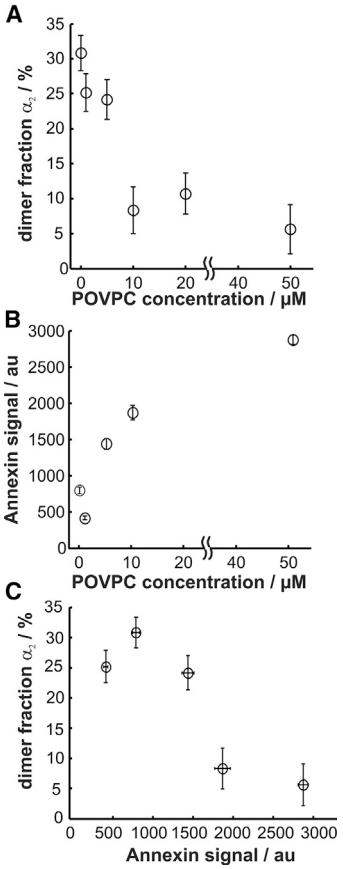

FIGURE 4 Dose effect of POVPC on mGFP-GPI nanoplatform integrity and apoptosis signal. CHO cells stably expressing mGFP-GPI were preincubated with different concentrations of POVPC for 20 min. (*A*) TOCCSL experiments were carried out at 37°C in the presence of POVPC and the dimer fraction was determined. The dimer fraction α_2 decreased monotonically with increasing concentrations of up to 10 μM POVPC and saturated above this concentration at values close to the detection limit of the TOCCSL technique. (*B*) The apoptosis signal of CHO cells was determined 30 min after oxPL incubation by using fluorescently labeled Annexin V and determined as a function of POVPC concentration in a plate-reader experiment. (*C*) The dimer fraction α_2 as a function of the Annexin V-Cy3 signal shows a negative correlation (correlation coefficient R = −0.88).

interaction of oxPLs with nanoplatforms in the plasma membrane leads to their disintegration and 2) an indirect mechanism involving downstream signaling initiated by oxPLs induces mGFP-GPI nanoplatform disruption. To discriminate between the two scenarios, we focused on a step during apoptosis signaling: the activation of aSMase (8). To inhibit aSMase activity, we used the inhibitor NB-19 (7) and preincubated mGFP-GPI-expressing CHO cells with 10 μM NB-19 for 30 min at 37°C. This agent inhibits aSMase, but not neutral sphingomyelinases, in macrophages, and exhibits an IC_{50} of 8 μM and <2 μM in stimulated macrophages and CHO cells, respectively. With 8 μM pretreatment (macrophages), the agent reduces minimally modified LDL-induced apoptosis by 75% (unpublished results, M. Blaess, University of Jena, and H.-P.D.). After inhibition, the cells were treated with 10 μM POVPC for 20 min and TOCCSL experiments were performed. Brightness analysis revealed an mGFP-GPI dimer fraction of 31% ± 4% (Fig. 5 *A*), which is nearly identical to the observed dimer fraction without the presence of oxPL. To test for a potential direct influence of NB-19 on mGFP-GPI nanoplatforms, we incubated cells with NB-19 alone. Analysis yielded nearly the same dimer fraction (30% ± 3%) as for the control (31% ± 3%). Thus, inhibition of aSMase completely abolished the effect of POVPC, and obviously the effect of oxPL on mGFP-GPI nanoplatform disintegration is strongly coupled to aSMase activity.

Finally, we were interested in finding out whether the standard test for raft-type interactions, namely, their dependence on plasma membrane cholesterol (20,33), could also be linked to aSMase activity. We thus performed TOCCSL experiments 20 min after addition of 2 U/mL COase at 37°C. A clear decrease in the mGFP-GPI dimer fraction down to 13% ± 4% was observed (Fig. 5 *B*). In contrast to POVPC experiments, a 30 min preincubation with NB-19 before COase treatment did not significantly influence the COase-induced reduction of the dimer fraction (10% ± 3%). We conclude that the mechanism for mGFP-GPI nanoplatform disintegration upon COase treatment does not involve aSMase activity.

DISCUSSION

Nanoplatforms containing GPI-anchored proteins are considered to be fundamental structural and functional units of the cell membrane (25). For example, oligomerization of a GPI protein was found to determine its sorting in polarized epithelial cells (19), and cross-linking of GPI proteins via antibodies is known to activate T cells (44,45). The Kusumi

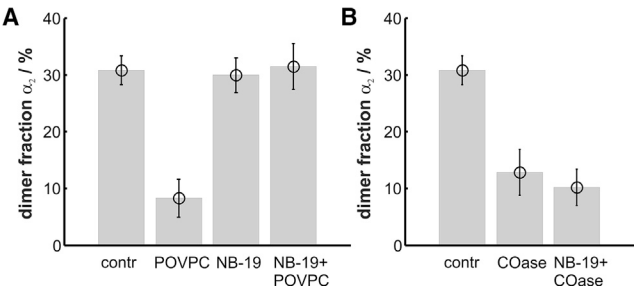

FIGURE 5 mGFP-GPI nanoplatform disintegration upon addition of oxPLs depends on aSMase activity. (*A*) CHO cells stably expressing mGFP-GPI were incubated with 10 μM POVPC for 20 min, either with (NB-19+POVPC) or without (POVPC) preincubation with the aSMase inhibitor NB-19 for 30 min at 37°C. TOCCSL experiments were carried out at 37°C in the presence of POVPC. Nanoplatform integrity could be conserved by inhibiting the activation of aSMase by preincubation with NB-19. Incubation with NB-19 alone (NB-19) had no effect on the observed nanoplatforms. (*B*) Nanoplatforms were dissolved by incubation with 2 U/mL of COase (COase). Inhibiting aSMase before COase (NB-19+COase) treatment did not inhibit nanoplatform disruption, thus pointing to a different mechanism for cholesterol-induced disintegration of mGFP-GPI nanoplatforms.

lab provided a detailed molecular picture of the recruitment of kinases to cross-linked GPI proteins and the subsequent initiation of downstream signaling events (18,46,47). Interestingly, cholesterol depletion abrogated both Lyn activation and the transient immobilization of the GPI-protein clusters (47), which was taken as an indication that cholesterol-based raft domains control the recruitment of cytosolic signaling proteins to GPI proteins. In a follow-up study, Suzuki et al. (18) found that both cholesterol-dependent raft-type interactions and ectodomain binding contribute to the association of GPI-anchored proteins. Apparently, nanoplatform integrity is critical for the initiation of signaling events via GPI proteins. Notably, most reported interventions that led to nanoplatform formation were induced by artificial agents, and only a couple of physiological stimuli were proven to trigger similar effects. Here, we addressed the question of how short-chain oxPLs (which are typically present in oxidatively modified LDL) affect nanoplatforms that host GPI-anchored proteins. We added oxPLs to an extent that reflects pathophysiological conditions, e.g., as found in carotid artery plaque samples (48). Our readout parameter was the homo-association of mGFP-GPI to stable nanoplatforms diffusing in the plasma membrane of live CHO cells (20). Upon addition of POVPC or PGPC, we found nearly complete disintegration of the mGFP-GPI nanoplatforms (Figs. 1 *F* and 2).

Given their rather unique shape, it would not be surprising to find that oxPLs have a strong impact on their environment in the plasma membrane, particularly on the distribution of cholesterol. In general, the mixing of lipids with cholesterol can be understood by means of the umbrella model, which assumes that the small polar head of cholesterol cannot directly cover the nonpolar steroid ring body, and therefore cholesterol relies on other phospholipids within the bilayer to cover its headgroup and enable integration (49). The umbrella effect becomes stronger for inverted-cone-shaped lipids such as oxPL and Lyso-PC, which provide an additional shielding area to cover the cholesterol. Indeed, recent MD simulations and dynamic light-scattering experiments showed pairing of oxPL species with cholesterol, similar to mixtures of lysolipid and cholesterol (13). Stefl et al. (14) also found that cholesterol stabilizes phospholipid model membranes containing oxPL by filling the void space caused by the truncated carbonyl chain. They even ascribed a healing role to cholesterol in the presence of oxidative damage. Along these lines, we could envision a scenario in which cholesterol preferentially associates with oxPL, thereby reducing the pool of freely diffusing cholesterol in the membrane, and ultimately causing an effect similar to that observed with cholesterol extraction. To test this hypothesis, we used a similarly inverted cone-shaped lysolipid instead of oxPL in our experiments. However, application of Lyso-PC did not lead to disintegration of the mGFP-GPI nanoplatforms (Fig. 2). Instead, we observed a minor increase in the dimer fraction, which may well have been caused by interexperiment variability due to slightly varying experimental and analytical conditions.

Several observations helped us to finally identify the mode of action of oxPL on plasma membrane nanoplatforms: 1) when we varied the POVPC concentration, we found a pronounced dose dependence of mGFP-GPI nanoplatform disintegration, which correlated with the onset of apoptosis probed with the specific marker Annexin V-Cy3, and 2) when we inhibited aSMase activity with NB-19 before addition of POVPC, we found that mGFP-GPI nanoplatforms remained stable in the plasma membrane and apoptosis was prevented (7). In other words, the mere presence of oxPL in the plasma membrane did not have any effect on the integrity of plasma membrane nanoplatforms. In fact, oxPL action was dependent on aSMase activity, which induces the generation of ceramide from sphingomyelin. A well-known functional consequence of ceramide production is the induction of apoptosis (reviewed in Mathias et al. (50)). In a previous study, Stemmer et al. (7) also detected surface exposure of PS in oxPL-treated RAW264.7 and bone-marrow-derived macrophages. This phenomenon could be causally related to the activation of aSMase because inhibition of this enzyme abolished the effect. In this study, we provide evidence that disintegration of the mGFP-GPI nanoplatform can also be prevented by inhibition of aSMase. Thus, the release of GPI-anchored protein homo-association is not directly mediated by the presence of POVPC in the plasma membrane; rather, it is a consequence of a process downstream of the initial POVPC-membrane interaction.

In addition, studies have reported that the membrane (nano-)structure is influenced by the presence of ceramide. In live cells, Lenne et al. (33) found a reduction in GFP-GPI confinement to microdomains upon treatment of cells with exogenously applied sphingomyelinase, and in model membranes, ceramide was shown to displace cholesterol from sphingomyelin-cholesterol domains (51,52). Moreover, ceramide forms distinct membrane domains (so-called ceramide-enriched membrane domains) that cluster and reorganize signaling molecules (reviewed in Grassmé et al. (53) and Zhang et al. (54)). In this study, we speculated that ceramide could directly cause mGFP-GPI nanoplatform disintegration. However, a more indirect mechanism due to a change in the plasma membrane cholesterol level upon aSMase activity also seems possible. Slotte et al. (55) showed that the degradation of plasma membrane sphingomyelin leads to redistribution of cholesterol, with less cholesterol in the plasma membrane and more in intracellular membranes. This loss of plasma membrane cholesterol could also cause our observed disintegration of mGFP-GPI.

Phenomenologically, these observations show similarities to our previous data that revealed disintegration of mGFP-GPI nanoplatforms upon treatment of CHO cells with COase (20), which is in line with multiple other studies on the cholesterol dependence of confinement and homodimerization of

GPI-anchored proteins (18,33,46,47,56). Interestingly, cholesterol-induced nanoplatform disintegration did not involve the action of aSMase (Fig. 5 *B*). Thus, it may well be that the two treatments have different modes of action, which happened to yield similar outcomes.

In summary, we have reported that oxPLs modified with aldehyde or carboxylic groups at the truncated chain disrupt plasma membrane nanoplatforms. In the case of aldehyde-modified oxPLs, we could link the disintegration to the activation of aSMase. The results are particularly interesting in view of the pathophysiological relevance of oxPLs in atherosclerosis and other inflammatory diseases: any signaling process that involves GPI proteins will be severely affected by the presence of oxPLs, which diminish the raft-type associations of these proteins.

SUPPORTING MATERIAL

One figure, one table, and Matlab Source code are available at http://www.biophysj.org/biophysj/supplemental/S0006-3495(15)01175-3.

AUTHOR CONTRIBUTIONS

M.B., E.S., A.H., and G.J.S. designed research. H.-P.D. and A.H. synthesized reagents. M.B., B.K.R., and C.M. performed microscopy experiments and analyzed data. B.P., M.P., and Z.T. performed MS experiments and analyzed data. M.B. and G.J.S. wrote the manuscript.

ACKNOWLEDGMENTS

We thank Elena Parkinson for assistance with cell culture.

This work was supported by Austrian Science Fund projects I307-B12, I301-B12, and I1953-B20, and by the Hungarian Basic Research Fund project OTKA ANN 112372.

REFERENCES

1. Deigner, H. P., and A. Hermetter. 2008. Oxidized phospholipids: emerging lipid mediators in pathophysiology. *Curr. Opin. Lipidol.* 19:289–294.
2. Stemmer, U., and A. Hermetter. 2012. Protein modification by aldehydophospholipids and its functional consequences. *Biochim. Biophys. Acta.* 1818:2436–2445.
3. Fruhwirth, G. O., A. Loidl, and A. Hermetter. 2007. Oxidized phospholipids: from molecular properties to disease. *Biochim. Biophys. Acta.* 1772:718–736.
4. Kinnunen, P. K., K. Kaarniranta, and A. K. Mahalka. 2012. Protein-oxidized phospholipid interactions in cellular signaling for cell death: from biophysics to clinical correlations. *Biochim. Biophys. Acta.* 1818:2446–2455.
5. Watson, A. D., N. Leitinger, …, J. A. Berliner. 1997. Structural identification by mass spectrometry of oxidized phospholipids in minimally oxidized low density lipoprotein that induce monocyte/endothelial interactions and evidence for their presence in vivo. *J. Biol. Chem.* 272:13597–13607.
6. Kolodgie, F. D., J. Narula, …, R. Virmani. 2000. Localization of apoptotic macrophages at the site of plaque rupture in sudden coronary death. *Am. J. Pathol.* 157:1259–1268.
7. Stemmer, U., Z. A. Dunai, …, A. Hermetter. 2012. Toxicity of oxidized phospholipids in cultured macrophages. *Lipids Health Dis.* 11:110.
8. Loidl, A., E. Sevcsik, …, A. Hermetter. 2003. Oxidized phospholipids in minimally modified low density lipoprotein induce apoptotic signaling via activation of acid sphingomyelinase in arterial smooth muscle cells. *J. Biol. Chem.* 278:32921–32928.
9. Rhode, S., R. Grurl, …, G. J. Schütz. 2009. Plasma membrane fluidity affects transient immobilization of oxidized phospholipids in endocytotic sites for subsequent uptake. *J. Biol. Chem.* 284:2258–2265.
10. Jurkiewicz, P., A. Olżyńska, …, M. Hof. 2012. Biophysics of lipid bilayers containing oxidatively modified phospholipids: insights from fluorescence and EPR experiments and from MD simulations. *Biochim. Biophys. Acta.* 1818:2388–2402.
11. Beranova, L., L. Cwiklik, …, P. Jungwirth. 2010. Oxidation changes physical properties of phospholipid bilayers: fluorescence spectroscopy and molecular simulations. *Langmuir.* 26:6140–6144.
12. Plochberger, B., T. Stockner, …, G. J. Schütz. 2010. Cholesterol slows down the lateral mobility of an oxidized phospholipid in a supported lipid bilayer. *Langmuir.* 26:17322–17329.
13. Khandelia, H., B. Loubet, …, M. Hof. 2014. Pairing of cholesterol with oxidized phospholipid species in lipid bilayers. *Soft Matter.* 10: 639–647.
14. Stefl, M., R. Sachl, …, M. Hof. 2014. Comprehensive portrait of cholesterol containing oxidized membrane. *Biochim. Biophys. Acta.* 1838:1769–1776.
15. Parkkila, P., M. Stefl, …, P. K. Kinnunen. 2015. Phospholipid lateral diffusion in phosphatidylcholine-sphingomyelin-cholesterol monolayers; effects of oxidatively truncated phosphatidylcholines. *Biochim. Biophys. Acta.* 1848 (1 Pt A):167–173.
16. Khandelia, H., and O. G. Mouritsen. 2009. Lipid gymnastics: evidence of complete acyl chain reversal in oxidized phospholipids from molecular simulations. *Biophys. J.* 96:2734–2743.
17. Fruhwirth, G. O., A. Moumtzi, …, A. Hermetter. 2006. The oxidized phospholipids POVPC and PGPC inhibit growth and induce apoptosis in vascular smooth muscle cells. *Biochim. Biophys. Acta.* 1761:1060–1069.
18. Suzuki, K. G., R. S. Kasai, …, A. Kusumi. 2012. Transient GPI-anchored protein homodimers are units for raft organization and function. *Nat. Chem. Biol.* 8:774–783.
19. Paladino, S., S. Lebreton, …, C. Zurzolo. 2014. Golgi sorting regulates organization and activity of GPI proteins at apical membranes. *Nat. Chem. Biol.* 10:350–357.
20. Brameshuber, M., J. Weghuber, …, G. J. Schütz. 2010. Imaging of mobile long-lived nanoplatforms in the live cell plasma membrane. *J. Biol. Chem.* 285:41765–41771.
21. Saka, S. K., A. Honigmann, …, S. O. Rizzoli. 2014. Multi-protein assemblies underlie the mesoscale organization of the plasma membrane. *Nat. Commun.* 5:4509.
22. Trullo, A., V. Corti, …, M. Zamai. 2013. Application limits and data correction in number of molecules and brightness analysis. *Microsc. Res. Tech.* 76:1135–1146.
23. Simons, K., and D. Toomre. 2000. Lipid rafts and signal transduction. *Nat. Rev. Mol. Cell Biol.* 1:31–39.
24. Horejsi, V., and M. Hrdinka. 2014. Membrane microdomains in immunoreceptor signaling. *FEBS Lett.* 588:2392–2397.
25. Kusumi, A., K. G. Suzuki, …, T. K. Fujiwara. 2011. Hierarchical mesoscale domain organization of the plasma membrane. *Trends Biochem. Sci.* 36:604–615.
26. Kusumi, A., T. K. Fujiwara, …, K. G. Suzuki. 2012. Dynamic organizing principles of the plasma membrane that regulate signal transduction: commemorating the fortieth anniversary of Singer and Nicolson's fluid-mosaic model. *Annu. Rev. Cell Dev. Biol.* 28:215–250.
27. Suzuki, K. G. 2012. Lipid rafts generate digital-like signal transduction in cell plasma membranes. *Biotechnol. J.* 7:753–761.

28. Schade, A. E., and A. D. Levine. 2002. Lipid raft heterogeneity in human peripheral blood T lymphoblasts: a mechanism for regulating the initiation of TCR signal transduction. *J. Immunol.* 168:2233–2239.
29. Fessler, M. B., and J. S. Parks. 2011. Intracellular lipid flux and membrane microdomains as organizing principles in inflammatory cell signaling. *J. Immunol.* 187:1529–1535.
30. Simons, K., and E. Ikonen. 1997. Functional rafts in cell membranes. *Nature.* 387:569–572.
31. Klotzsch, E., and G. J. Schütz. 2013. A critical survey of methods to detect plasma membrane rafts. *Philos. Trans. R. Soc. Lond. B Biol. Sci.* 368:20120033.
32. Sevcsik, E., M. Brameshuber, …, G. J. Schütz. 2015. GPI-anchored proteins do not reside in ordered domains in the live cell plasma membrane. *Nat. Commun.* 6:6969.
33. Lenne, P. F., L. Wawrezinieck, …, D. Marguet. 2006. Dynamic molecular confinement in the plasma membrane by microdomains and the cytoskeleton meshwork. *EMBO J.* 25:3245–3256.
34. Sharma, P., R. Varma, …, S. Mayor. 2004. Nanoscale organization of multiple GPI-anchored proteins in living cell membranes. *Cell.* 116:577–589.
35. Goswami, D., K. Gowrishankar, …, S. Mayor. 2008. Nanoclusters of GPI-anchored proteins are formed by cortical actin-driven activity. *Cell.* 135:1085–1097.
36. Raghupathy, R., A. A. Anilkumar, …, S. Mayor. 2015. Transbilayer lipid interactions mediate nanoclustering of lipid-anchored proteins. *Cell.* 161:581–594.
37. Varma, R., and S. Mayor. 1998. GPI-anchored proteins are organized in submicron domains at the cell surface. *Nature.* 394:798–801.
38. Zacharias, D. A., J. D. Violin, …, R. Y. Tsien. 2002. Partitioning of lipid-modified monomeric GFPs into membrane microdomains of live cells. *Science.* 296:913–916.
39. Moertelmaier, M., M. Brameshuber, …, H. Stockinger. 2005. Thinning out clusters while conserving stoichiometry of labeling. *Appl. Phys. Lett.* 87:263903.
40. Schmidt, T., G. J. Schütz, …, H. Schindler. 1996. Local stoichiometries determined by counting individual molecules. *Anal. Chem.* 68:4397–4401.
41. Brameshuber, M., and G. J. Schütz. 2012. Detection and quantification of biomolecular association in living cells using single-molecule microscopy. *Methods Enzymol.* 505:159–186.
42. Antal, O., M. Péter, …, L. G. Puskás. 2015. Lipidomic analysis reveals a radiosensitizing role of gamma-linolenic acid in glioma cells. *Biochim. Biophys. Acta.* 1851:1271–1282.
43. Martin, S. J., C. P. Reutelingsperger, …, D. R. Green. 1995. Early redistribution of plasma membrane phosphatidylserine is a general feature of apoptosis regardless of the initiating stimulus: inhibition by overexpression of Bcl-2 and Abl. *J. Exp. Med.* 182:1545–1556.
44. Stefanová, I., V. Horejsí, …, H. Stockinger. 1991. GPI-anchored cell-surface molecules complexed to protein tyrosine kinases. *Science.* 254:1016–1019.
45. Lipp, A. M., K. Juhasz, …, A. Sonnleitner. 2014. Lck mediates signal transmission from CD59 to the TCR/CD3 pathway in Jurkat T cells. *PLoS One.* 9:e85934.
46. Suzuki, K. G., T. K. Fujiwara, …, A. Kusumi. 2007. Dynamic recruitment of phospholipase C gamma at transiently immobilized GPI-anchored receptor clusters induces IP3-Ca2+ signaling: single-molecule tracking study 2. *J. Cell Biol.* 177:731–742.
47. Suzuki, K. G., T. K. Fujiwara, …, A. Kusumi. 2007. GPI-anchored receptor clusters transiently recruit Lyn and G alpha for temporary cluster immobilization and Lyn activation: single-molecule tracking study 1. *J. Cell Biol.* 177:717–730.
48. Davis, B., G. Koster, …, A. D. Postle. 2008. Electrospray ionization mass spectrometry identifies substrates and products of lipoprotein-associated phospholipase A2 in oxidized human low density lipoprotein. *J. Biol. Chem.* 283:6428–6437.
49. Huang, J., and G. W. Feigenson. 1999. A microscopic interaction model of maximum solubility of cholesterol in lipid bilayers. *Biophys. J.* 76:2142–2157.
50. Mathias, S., L. A. Peña, and R. N. Kolesnick. 1998. Signal transduction of stress via ceramide. *Biochem. J.* 335:465–480.
51. Megha, and E. London. 2004. Ceramide selectively displaces cholesterol from ordered lipid domains (rafts): implications for lipid raft structure and function. *J. Biol. Chem.* 279:9997–10004.
52. Megha, O. B., O. Bakht, and E. London. 2006. Cholesterol precursors stabilize ordinary and ceramide-rich ordered lipid domains (lipid rafts) to different degrees. Implications for the Bloch hypothesis and sterol biosynthesis disorders. *J. Biol. Chem.* 281:21903–21913.
53. Grassmé, H., J. Riethmüller, and E. Gulbins. 2007. Biological aspects of ceramide-enriched membrane domains. *Prog. Lipid Res.* 46: 161–170.
54. Zhang, Y., X. Li, …, E. Gulbins. 2009. Ceramide-enriched membrane domains—structure and function. *Biochim. Biophys. Acta.* 1788: 178–183.
55. Slotte, J. P., G. Hedström, …, S. Ekman. 1989. Effects of sphingomyelin degradation on cell cholesterol oxidizability and steady-state distribution between the cell surface and the cell interior. *Biochim. Biophys. Acta.* 985:90–96.
56. Eggeling, C., C. Ringemann, …, S. W. Hell. 2009. Direct observation of the nanoscale dynamics of membrane lipids in a living cell. *Nature.* 457:1159–1162.